UCRL-TR-216963

LAWRENCE
LIVERMORE
NATIONAL
LABORATORY

Experimental and Modeling Characterization of PETN Mobilization Mechanisms During Recrystallization at Ambient Conditions

A. K. Burnham, R. Gee, A. Maiti, R. Qiu, P. Rajasekar, B. Weeks, L. Zepeda-Ruiz

November 9, 2005

Disclaimer

This work was performed under the auspices of the U.S. Department of Energy by University of California, Lawrence Livermore National Laboratory under Contract W-7405-Eng-48.

Experimental and Modeling Characterization of PETN Mobilization Mechanisms During Recrystallization at Ambient Conditions

Alan Burnham,[a] Richard Gee,[a] Amitesh Maiti,[a] Roger Qiu,[a] Pitchmani Rajasekar,[b]
Brandon Weeks,[b] Luis Zepeda-Ruiz[a]

Lawrence Livermore National Laboratory, Chem. and Mat. Sci., Livermore, CA 94550
Texas Tech University, Dept. of Chem. Eng., Lubbock, TX 79409

Introduction

Experimental measurements suggest that pentaerythritoltetranitrate (PETN) undergoes changes at the molecular level that cause macroscopic changes in the overall PETN powder characteristics over time. These changes have been attributed to the high molecular mobility of PETN, but the underlying mechanism(s) responsible for this redistribution are still uncertain. Two basic approaches have been implemented in the past year to provide insight into the nature of these underlying mechanisms. The first approach is of an experimental nature, utilizing both AFM and evaporation measurements, which address both surface mobility and evaporation. These data include AFM measurements performed at LLNL and evaporation rate measurements performed at Texas Tech. These results are compared to earlier vapor pressure measurements performed at SNL, and estimates of recrystallization time frames are given. The second approach utilizes first-principle calculations and simulations that will be used to compare directly to those experimental quantities measured. We are developing an accurate inter-molecular potential for PETN, which via kinetic Monte Carlo (KMC) simulations would mimic real crystallite shapes. Once the basic theory is in place for the growth of single crystallites, we will be in a position to investigate realistic grain coarsening phenomena in multi-crystallite simulations. This will also enable us to study how to control the morphological evolution, e.g., through thermal cycling, or through the action of custom additives and impurities.

1. A Brief Summary of the Experimental Findings

Experimentally, we find that PETN is quite mobile. Surface rearrangement and possibly evaporation is observed by AFM for single crystals at temperatures as low as 30 ^{o}C. Measurement of step velocities from 30 to 50 ^{o}C gives an activation energy of 33.4 kcal/mol, which in the lower range measured by Behrens [1] for the enthalpy of evaporation. Estimation of the step density on the crystal surface gives an estimated total mobility rate that implies that most of the crystal might reorganize over the course of a year. However, this does not take into account the pinning of bunched steps and that the thermodynamic driving force for recrystallization might decline over time. Our modeling activities, however, intend to be used here to address issue of this nature (see Figure 15 below). Measurement of evaporation rates by TGA leads to a similar activation energy, but the total mobility rate is about 400 times lower than estimated from AFM data. Calculations of evaporation rates using the vapor pressure and the ideal gas law for diffusion are qualitatively consistent with observed TGA measurements. Additional calculations suggest that about 2% of the PETN might be expected to recrystallize during a year at 30 ^{o}C.

The driving force for recrystallization is related to the difference in free energy of the starting and final crystals. Ordinarily, high-temperature annealing is a deceleratory process, where the least stable crystals evaporate and recrystallize on more stable crystals. However, a longer-term mechanism is identified in which there is an induction time for the formation of a few small, perfect crystals, which subsequently grow at an increasing rate as their surface area increases.

1.1 AFM Mobility Measurements

Relatively large (~1 mm in length) PETN single crystals were grown from supersaturated organic solution via a solvent evaporation method at a temperature of 5 °C. Representative crystals are shown in Figure 1. Although x-ray diffraction analysis was not performed, all crystals had the typical habit of single crystal PETN. The crystals were used as samples for surface evolution studies via Atomic Force Microscopy (AFM).

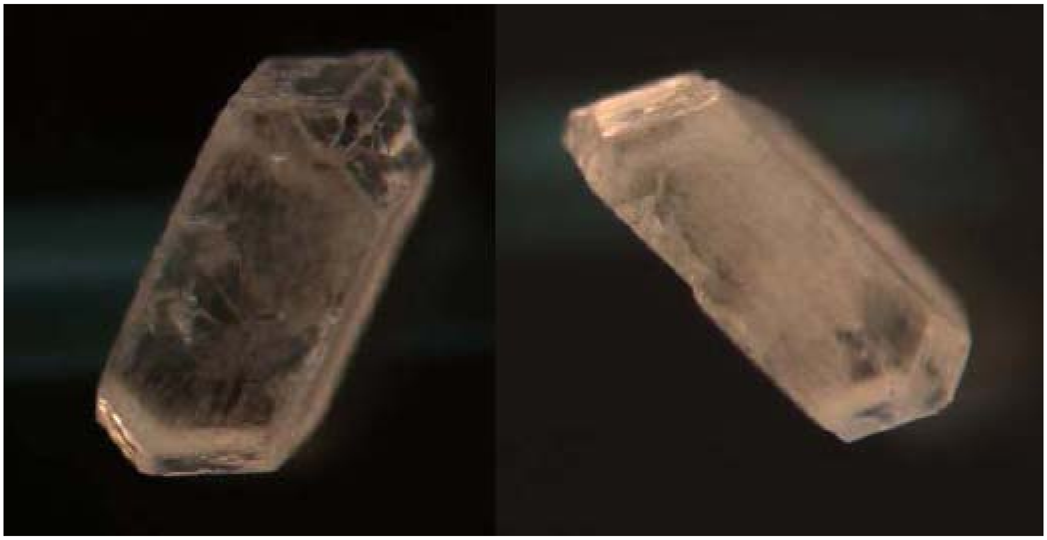

Figure 1. PETN single crystals grown from supersaturated solution via solvent evaporation at 5 °C.

Surface morphologies of PETN of {110} plane at a range of temperatures (22-50 °C) were investigated using in-situ AFM at ambient pressure in an open environment. The sample was heated by a commercially available resistive-heating stage. By monitoring the changes in surface modification as a function of time at different temperatures, we determined an Arrhenius relationship for the step velocity. The combination of disappearance of islands and growth of pits suggests that the dominant driving force for mobility is evaporation, although alternative explanations are discussed later. A sequence of AFM micrographs is shown in Figure 2, and both island shrinkage and pit growth are evident.

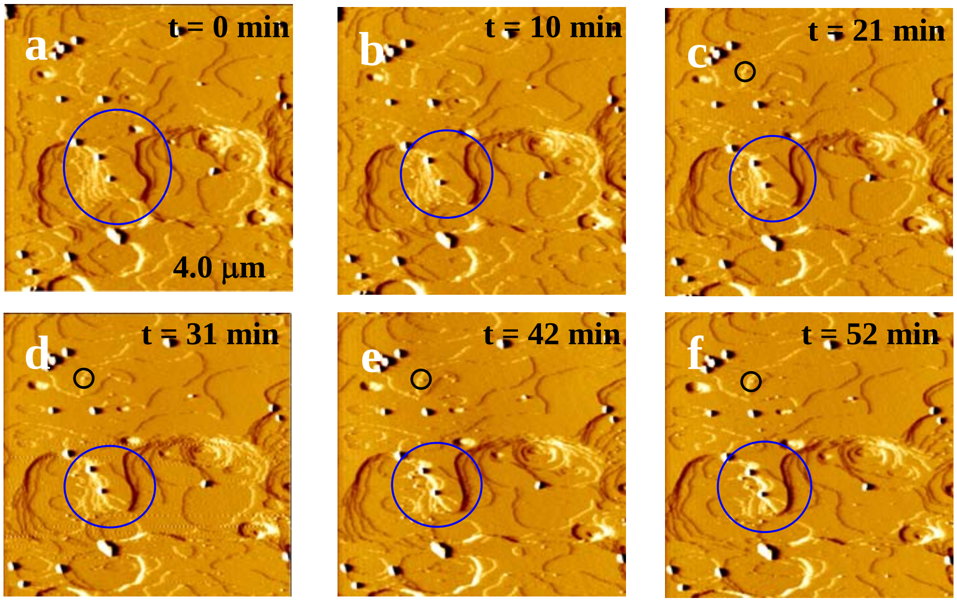

Figure 2. Change in surface topography as a function of time for the (110) face of a PETN crystal heating to 30 °C.

A program was written to identify step edges and calculate areas of islands and pits on otherwise relatively step-free portions of the surface, and an equivalent radius of the island or pit was calculated from those areas. Diameters of additional pits were measured manually. The resulting plots of diameter vs. time are given in Figure 3. The plots for the island shrinkage, in particular, are very linear. The slopes of these plots give a step velocity, and those step velocities when plotted versus reciprocal temperature yield an activation energy, as shown in Figure 4. There is a considerable falloff for the pits at 50 °C, but the other data forms a clear trend. An Arrhenius fit to the island shrinkage data give A=5.36×10^{15} cm/s and E=33.40 kcal/mol.

To calculate an "evaporation" rate, one also needs the areal density of step edges on the crystal, along with the assumption that all edges move at the same rate. A rough estimate of step density was derived by drawing straight line segments over the steps of one micrograph, as shown in Figure 5, and then adding the length of these line segments. This yielded a step density of 5.8 $\mu m/\mu m^2$, or 5.8×10^4 cm/cm^2, which is probably accurate to within a factor of a few, not considering step bunching. Assuming a cubic lattice and a molecular diameter of 0.67 nm, the each layer weighs 1.17×10^{-7} g/cm^2. Multiplying the rate constant above by the areal step and mass densities gives k= $3.64\times10^{13}\exp(-16811/T)$ $g/s/cm^2$, or $2.18\times10^{16}\exp(-16811/T)$ $mg/min/mm^2$, for mass movement in ambient air.

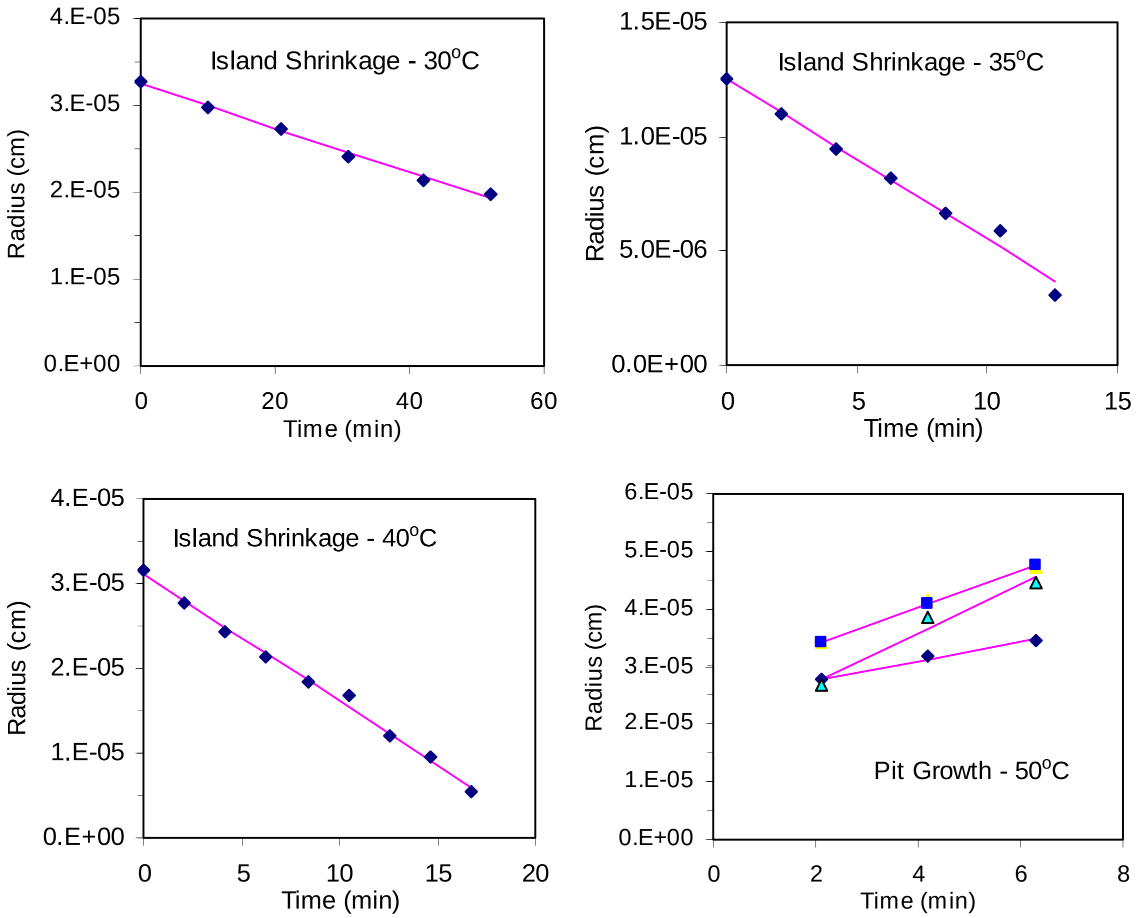

Figure 3. Plots of effective radii of islands and pits as a function of time at different temperatures. Three separate cases are shown for pits at 50 °C, and the zero time is not distinct enough for accurate measurement.

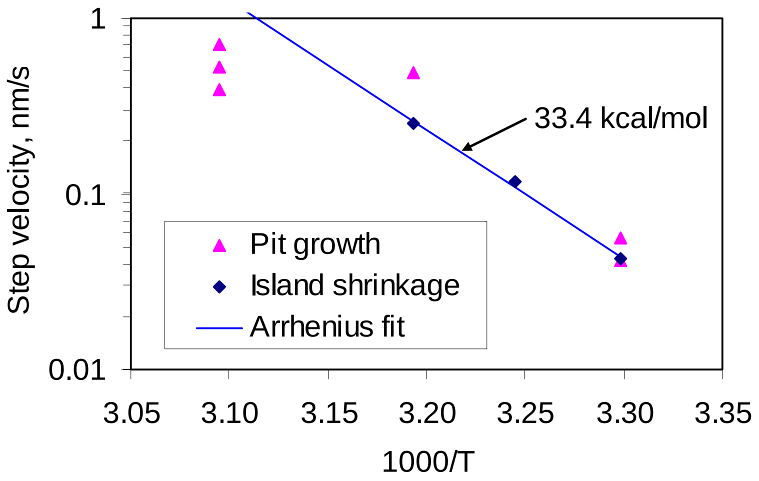

Figure 4. Arrhenius plot of step velocities for pit growth and island shrinkage. The Arrhenius fit is to the island shrinkage data only.

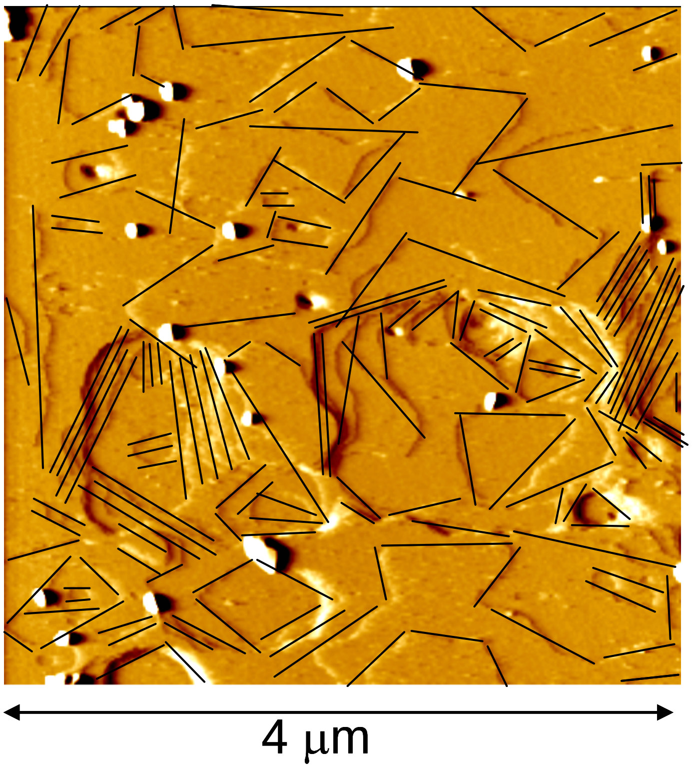

Figure 5. Method used to estimate the step density on a PETN crystal. Line segments approximately covered all step edges and were then moved into a smaller set of lines, from which subtotal lengths were estimated. The total step length here is 92.8 μm in a 16 μm^2 area.

1.2 TGA Evaporation Measurements

Crystals for mass loss rate measurements were grown over a period of several weeks by the solvent evaporation technique. One such crystal is shown in Figure 6. XRD and IR measurements confirmed that the crystals were pure PETN. Individual crystals were heated at temperatures from 110 to 135 ^{o}C in a carefully calibrated thermogravimetric apparatus. The rate of mass loss was normalized to exposed surface area, and Arrhenius rate parameters were derived from plots such as in Figure 7. The activation energies derived from these experiments is within experimental error to that reported in the preceding section for AFM mobility and is at the lower end of the range of vaporization enthalpies reported by Behrens [1]. The experiment was done at multiple gas flow rates to assess the contribution of boundary-layer resistance to the evaporation rate. The evaporation rate is 26% faster at 60 ^{o}C and 34% faster at 130 ^{o}C for the fourfold higher flowrate, indicating a small but detectable boundary-layer resistance.

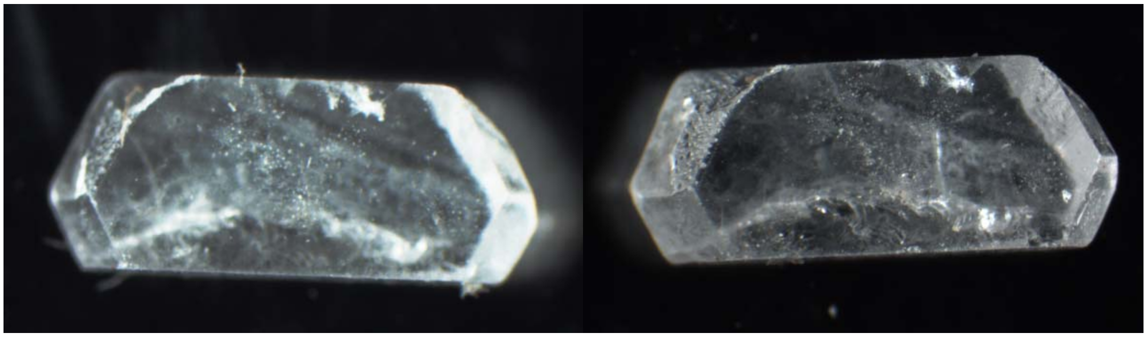

Figure 6. A 4-mm-long PETN crystal as grown (left) and after low-temperature heating at 40 °C (right). The heating tends to reduce surface roughness and scattering with no apparent mass loss.

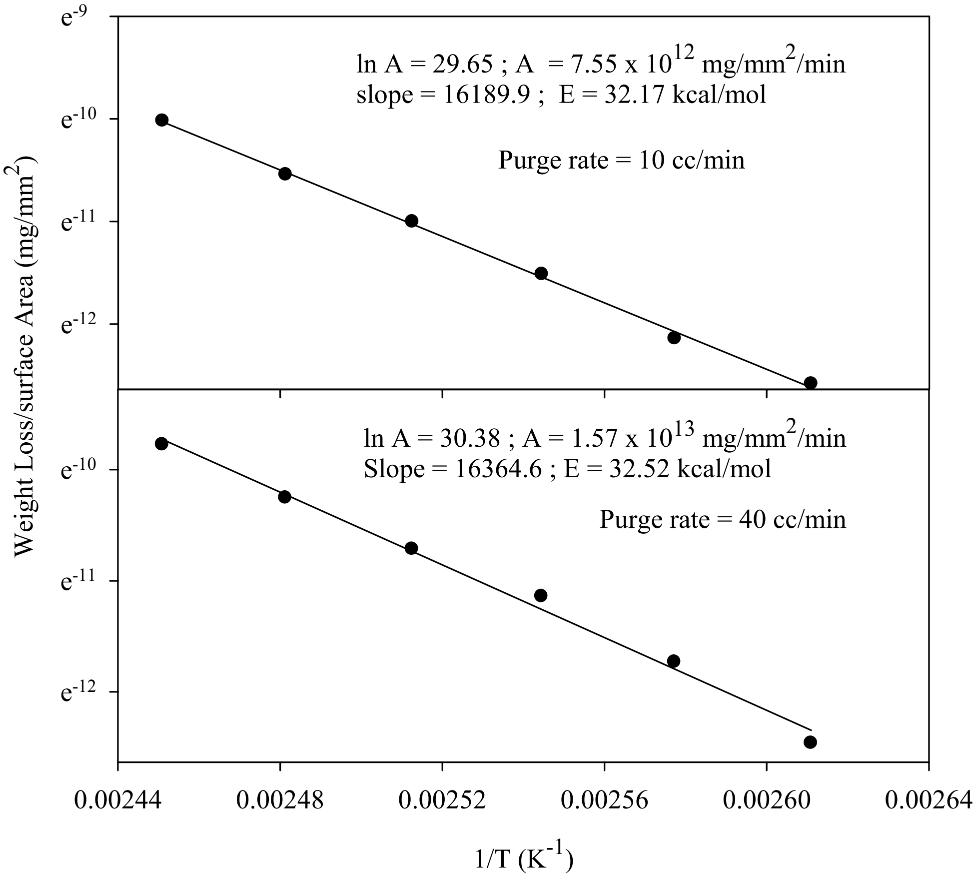

Figure 7. Rate of mass loss per unit exposed surface area as a function of reciprocal temperature.

1.3 Comparison of AFM and TGA Measurements

Another interesting comparison is the relative rates of the AFM and TGA experiments over the complete temperature range. This is shown in Table 1. The AFM rates are about 400 times orders of faster than the TGA rates. Because the activation energies are similar, the ratio changes only slightly over the temperature range. Part of the discrepancy may be due to the quality of crystal (defect density and steps per unit area). If the AFM truly represents vaporization and not merely diffusion of mass to another part of the crystal, one might also consider differences in boundary layer resistance. However, the TGA experiments used an active gas flow and found only a minor dependence on gas flow rate, so that is not a likely explanation.

More likely is that the AFM measures more than vaporization, the estimation of the density of active steps is too high, or the density of steps is higher on the AFM crystal, or some combination of the three. One issue is that the AFM kinetic expression actually applies to what we believe are single steps. However, much of the observed topography is associated with multiple steps, and that is ignored in the step density measurement in Figure 5. Bunched steps are likely to have a substantially lower velocity—lower by a larger factor than the number of steps in the bunch. This would mean that the estimation of mobile step density could be too high by an order of magnitude or so. The other possibility, that we are observing surface reorganization rather than evaporation, is more difficult to assess. The Texas Tech crystals were observed to become smoother with low-temperature aging, but this rearrangement is probably on a longer distance scale than can be assessed by AFM. If AFM mobility is really dominated by surface diffusion, surface diffusion must be actively considered in any aging process.

Table 1. Comparison of evaporation rates (g/cm^2/min) from LLNL AFM measurements and Texas Tech TGA measurements. Calculates within the range of measurement are in bold.

Temperature, ^{o}C	AFM	TGA	AFM/TGA
30	**1.8×10^{-9}**	5.6×10^{-12}	320
40	**1.1×10^{-8}**	3.2×10^{-11}	335
60	2.7×10^{-7}	7.3×10^{-9}	365
80	4.6×10^{-6}	1.2×10^{-8}	394
100	5.9×10^{-5}	**1.4×10^{-7}**	421
120	5.9×10^{-5}	**1.3×10^{-6}**	448
140	4.6×10^{-3}	**9.8×10^{-6}**	473

The activation energies from AFM and TGA can be compared to the enthalpy of evaporation. The activation energy for evaporation is equal to the enthalpy of sublimation minus RT, so the TGA and vapor pressure energies should be within 1 kcal/mol of the enthalpy. The TGA value of 32.5 kcal/mol is on the low end of the vapor pressure enthalpy range of 32-40 kcal/mol reported by Behrens [1], as it should be. The AFM activation energy (33.4 kcal/mol) is also slightly lower than the vapor pressure enthalpy. This lower value could be due to either a lower value for an imperfect crystal or a dominant contribution of surface diffusion to the AFM measurement.

1.4 Modeling of Evaporative Recrystallization

The rate of vaporization of any material depends on the surrounding pressure. Even thought the vapor pressure of a material is independent of other gases, the presence of another gas slows the transport of the vaporizing molecule from the surface. Consequently, gaseous diffusion away from the surface can become the rate limiting step.

In a vacuum, the molar flux away from the surface is given by

$$J = p/(2\pi MRT)^{1/2} \tag{1}$$

where p is the vapor pressure, M is the molecular weight, R is the gas constant, and T is the absolute temperature.

In the presence of a foreign gas, the molar flux is instead given by

$$J = pD_{12}/(zRT) \tag{2}$$

Where D_{12} is the mutual diffusion constant for the molecule of interest in the foreign gas, and z is the distance from the evaporating surface where the partial pressure of evaporating gas drops to zero.

For evaporation in either vacuum or a foreign gas, the net flux between two crystals will be zero if the vapor pressures are equal. If one crystal is more stable, hence has a lower vapor pressure, the net rate of transport will be related to the differences in vapor pressure, which in turn are related to the differences in free energies:

$$\Delta p = p_1 - p_2 = \exp(-\Delta G_1) - \exp(-\Delta G_2) \tag{3}$$

The self diffusion constant, D, of a pure gas is proportional to its mean free path

$$\lambda = 1/(2^{1/2}\pi d^2 C) \tag{4}$$

times the average velocity,

$$u = (8RT/\pi M)^{1/2} \tag{5}$$

which gives a formula in terms of molecular constants of

$$D = \lambda u/3 = \frac{2(RT)^{1/2}}{3\pi^{3/2}M^{1/2}d^2C} \tag{6}$$

where M is the molecular weight (g/mole), d is the molecular diameter (cm), C is the concentration (molecules/cm^3), and R is 8.314×10^7 ergs/mol/K and 1 erg = 1 g cm^2/s^2. At 0 ^{o}C and atmospheric pressure, the concentration is one mole per 22.414 liters, or 2.69×10^{19} molecules/cm^3.

Table 2 summarizes the vapor pressure and mean free path for PETN in a vacuum. Pure vapor diffusion and mutual diffusion (in air) constants are estimated in

Table 2 for PETN using the vapor pressure measurements of Behrens [1], which are described by $p = 8.5\times10^{17} \exp(-17675/T)$ torr. The PETN molecular diameter was estimated as 0.67 nm from the crystal density of 1.76 g/cm^3, which gives an air-PETN collisional diameter of 0.5 nm. Over this temperature range, the pure vapor pressure is low enough that the mean free path is much larger than the pore diameters in powders of interest. This condition means that the mechanism would be Knudsen diffusion. For comparison, the mean free path of air at atmospheric pressure is about 1×10^{-5} cm, or 100 nm, which is smaller than most pore diameters.

Table 2. Diffusion constants of PETN

T, °C	p, torr	λ (at v.p.), cm	D (at v.p.), cm^2/s	λ (1 atm air), cm	D_{12} (in air), cm^2/s
30	4.0×10^{-8}	3.60×10^{4}	1.7×10^{8}	9.3×10^{-6}	7.2×10^{-3}
45	6.3×10^{-7}	2.40×10^{3}	1.2×10^{7}	9.8×10^{-6}	7.8×10^{-3}
60	3.2×10^{-5}	1.98×10^{2}	9.9×10^{5}	1.03×10^{-5}	8.3×10^{-3}
75	7.9×10^{-5}	2.09×10^{1}	1.1×10^{5}	1.07×10^{-5}	8.9×10^{-3}
90	5.9×10^{-4}	2.92×10^{0}	1.5×10^{4}	1.12×10^{-5}	9.5×10^{-3}

Now consider the case where a few heavy molecules (e.g., PETN = 316 amu) are evaporating and diffusing through a sea of light gases (e.g., air ~ 29 amu). The mean free path of PETN in air is about 5× smaller than for air itself because of its larger cross-section, so transport would occur by gaseous diffusion rather than Knudsen diffusion. The mutual diffusion coefficient of PETN in air is given by

$$D_{12} = \frac{1}{3\pi} \frac{u_1}{C_1 d_1^2 \sqrt{2} + C_2 d_{12}^2 [1 + (M_1 / M_2)]^{1/2}} \qquad (7)$$

where subscript 1 refers to PETN and subscript 2 refers to air. The bimolecular collision diameter, d_{12}, is assumed to be 0.5 nm. The calculated mutual diffusion is given in Table 2.

The measured TGA evaporation rate can be compared to that calculated from the vapor pressure for various assumptions of boundary layer resistance. Eq. 2 assumes that the vaporization rate is very fast next the solid interface and the flux is limited by diffusion to the distance of negligible partial pressure. Using R=82.06 cm^{3}atm/mole/K and multiplying the molar flux by the molecular weight, we obtain fluxes of 4.8×10^{-12}, 1.0×10^{-19}, and 3.1×10^{-7} g/cm^2/s at 30, 60, and 100 °C, respectively, for a 10 µm diffusion length. These are approximately equal to what is observed in the TGA measurements. Given that the dependence of vaporization rate on gas flow rate, the boundary layer must be small, so this is a reasonable comparison.

We now turn to the transfer of PETN from one crystal to another. The average distance, x, a given molecule can diffuse in time, t, is given by

$$x = (2D_{12}t)^{1/2} \qquad (8)$$

Diffusion constants from Table 2 indicate that a vapor molecule moves 7-8 cm on average in an hour, essentially independent of temperature over the range of interest. This is not to say that the rate of transfer to a cold sink is independent of temperature, because the flux depends on the density of molecules in addition to the diffusion rate. However, we can conclude for long-term aging that the rate of deposition on a growing crystal is basically limited by the frequency of gas collisions on that crystal surface, which is proportional to vapor pressure, along with the sticking coefficient, and not the diffusion constant.[1] The frequency of collision, f, between a gas and a surface is given by

$$f = C_1 u_1 / 4. \tag{9}$$

Over the range of temperatures in Table 2, the collisional frequency increases from 4.5×10^{12} to 6.1×10^{16} molecules/s/cm^2.

PETN has a density of 1.76 g/cm^3 and a molecular weight of 316 g/mole, so its crystal density is 3.35×10^{21} molecules/cm^3. Dividing the collisional frequency by this density indicates that for 100% sticking, the growth velocity increases from 0.01 to 183 nm/s as temperature increases from 30 to 90 $^{\circ}$C. Assuming that the growing crystal has negligible vapor pressure compared to the source, it would take about a minute at 30 $^{\circ}$C for each molecular layer, assuming a molecular layer thickness of 0.67 nm. The total growth over one year ranges from 430 μm at 30 $^{\circ}$C to 5.8 m at 90 $^{\circ}$C. Clearly, the rate of availability of PETN vapor to a growing surface is not a significant limiting factor for recrystallization.

In any real crystal redistribution situation, the net rate of transfer from one crystal to another is proportional to the differences in vapor pressure or other mobility mechanism, which is proportional to the difference in free energy of the two crystalline forms, i.e., Eq. (3). The difference could show up in both the enthalpy and entropy contributions. For example, Rogers and Dinegar found up to a 20% difference in heats of fusion of PETN crystallized under different conditions, which was a much greater difference than increasing surface area by grinding. Also, Behrens typically found, during thermal cycling, an increase in the enthalpy of evaporation from ~34 to ~39 kcal/mol for thermally stabilized powders. This could be due to selective evaporation, annealing, or both, and perfect crystals may have an enthalpy at the high end of the observed range. The absolute value of the vapor pressure decreased by about 3× over a few cycles, so one might expect a perfect crystal to have a ~5× lower vapor pressure than a typical starting powder. The vapor pressure of powder B1084 decreases by a greater amount during thermal cycling than does powder K1202, so it might be expected to recrystallize faster. After three cycles, they have a similar vapor pressure.

The practical implications of these observations is that one might expect the initial driving force for vapor-phase recrystallization to be a few times the vapor pressure of a perfect crystal, and over time, the driving force would decay to a fraction of the vapor

---

[1] Artificial aging experiments in which the diffusion time across the sample is not short compared to the time of the experiment might give misleading results because of the contribution of diffusion limitations to the mass transfer rate. This might be a concern for high-temperature aging experiments.

pressure of a perfect crystal. One might assume a Winnebago is close to a perfect crystal. The vapor pressures given in Table 2 are for after thermal cycling, so they are presumably more representative of perfect crystals.

We now return to the issue of the rate of potential recrystallization. Preceding calculations assumed that the vaporization kinetics were fast and that the rate of recrystallization depended only on the collision frequency on the growing crystal face for the equilibrium vapor pressure. Now let's consider the total rate of evaporation for a powder having a surface area of 6000 cm^2/g. Multiplying the AFM and TGA rates by this surface area gives total fluxes at 30 ^oC of 1.1×10^{-5} and 3.3×10^{-8} g vapor/g sample/min, respectively. There are 5.3×10^5 minutes in a year, so the AFM rate implies that essentially all the sample could recrystallize in that time frame if the movement were perfectly efficient. Obviously, that is not true. Of course, intergrain transfer would be limited by the contact surface area. The TGA rate is consistent with 1.8% of the sample being vaporized over the course of the year, which is within the plausible range.

Given this first stage of analysis, one would expect PETN to undergo substantial recrystallization if the free energy of the starting crystal form deviates substantially from the ideal value. If the starting crystals are thermodynamically unstable compared to a perfect crystal, one might expect both selective evaporation of the most unstable powder at the beginning and its redeposition on more stable crystals. Some crystal annealing might also occur. In the longer term, the rate limiting step for ultimate recrystallization may be the nucleation of a perfect crystal (or crystals) that would eventually suck up all available PETN. This would lead to an induction time for surface area reduction and an acceleratory rate as the surface area of these perfect crystals increases with time.

2. Brief Summary of PETN Modeling Effort

A new forcefield has been generated that matches experimental crystal energies and structure. Kinetic Monte Carlo calculations using this forcefield have shown that some differences in crystal shape (asymmetry) can be attributed to the statistical nature of the growth process while others (length to width) are related to the probability of diffusion, which scales as temperature. We are making progress on explaining the activation energies of various steps in diffusion and evaporation, and we have started to simulate the ripening of particle assemblies.

2.1 Development of an "on-lattice" inter-molecular potential

Fig. 8(a, b) respectively displays the equilibrium structure of a PETN molecule optimized by the COMPASS forcefield [2], and the experimental crystal structure of PETN [3]. The H-atom positions in the experimental crystal structure, which cannot be easily deciphered from X-ray crystal data, were optimized by COMPASS as well. The lattice energy (normalized per molecule) E_{Lat} of this structure is readily computed as -

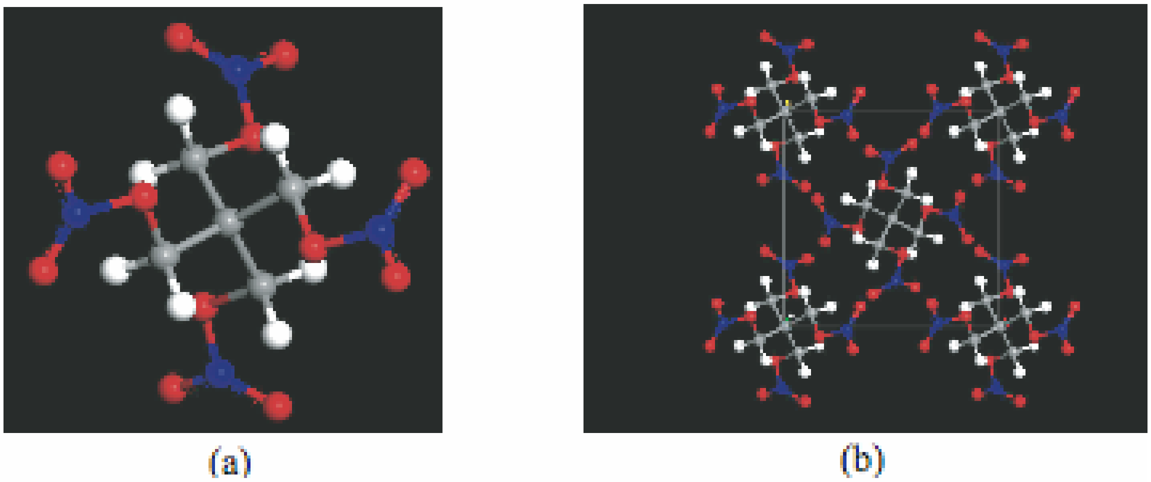

Figure 8. (a) PETN Molecule; (b) Experimental crystal structure of PETN.

38.8 kcal/mol, which agrees quite well with an experimental value of -36.3 kcal/mol [4, 5]. One could start from this structure and readily obtain the average growth morphology [6] or crystal "habit" as shown in Fig. 9 (a). In the computed morphology the crystal habit appears elongated along the z-axis being flanked by the four {110} facets along its length, while the end caps are facetted by eight planes belonging to the {101} family. The experimental morphology also appears to be dominated by these two families of facets (a "typical" crystallite being shown in Fig. 9(b)). However, most of the experimental particles deviate from the nice symmetry of Fig. 9(a). For instance, although all crystallites are elongated along the crystal Z-axis, the ratios of surface area of the {110} to the {101} facets vary significantly from crystallite to crystallite, and the areas of end {101} faces are typically unequal within the same crystallite. To obtain more realistic growth morphologies, our plan was to carry out simulations starting from an arbitrary initial shape of a seed particle and subject it to a large number of particle addition and MC diffusion moves.

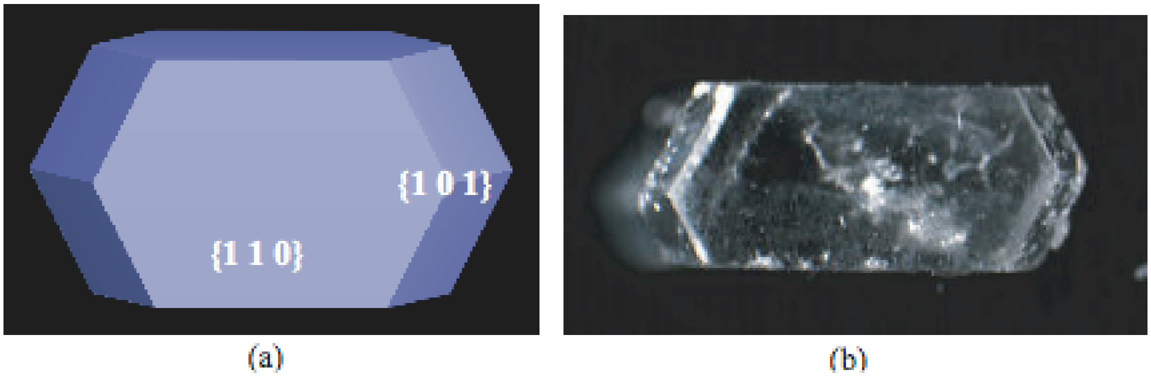

Figure 9. PETN crystal growth morphology: (a) computed; (b) typical experimental morphology.

As a prelude to MC simulations we carried out several Classical MD simulations on both {110} and {101} facets. We found that if we add an extra PETN molecule at an arbitrary orientation to a surface cleaved from the experimental bulk structure, the molecule quickly snaps into the nearest lattice position in the same orientation as a PETN molecule in crystal lattice should be. This provided justification that one could consider a molecule as a basic entity and use an effective molecule-molecule interaction potential defined from the bulk lattice. Furthermore, since a PETN molecule does not carry a net charge or a dipole moment, it is reasonable to assume that such a potential would fall off fast enough, so that one could justifiably limit energy computation only to the first few neighbors. To quantify the rate of this fall-off, we note that the lattice energy can be written as a sum of such potential over all neighbor shells, i.e.,

$$E_{Lat} = \frac{1}{2}\sum_{i=1}^{\infty} Z_i E_{MM}(i) + \Delta E ,$$

where $E_{MM}(i)$ is the molecular interaction energy between ith neighbors (i.e. neighbors belonging to the ith shell), Z_i is the number of ith neighbors, and ΔE is a positive number denoting the energy of relaxation of an isolated molecule from its structure in the bulk lattice. It is therefore desired that not only $E_{MM}(i)$ falls off fast with i, but so does the difference of the total E_{Lat} from the the cumulative contribution to E_{Lat} due to all neighbors on and within the i^{th} shell, given by

$$E_{cum}(i) = \frac{1}{2}\sum_{j=1}^{i} Z_j E_{MM}(j) + \Delta E .$$

Table 3 displays such an interaction potential (E_{MM}) and E_{cum} for the first five neighbors, and shows that it would be good approximation to cut off the potential beyond the fourth or fifth nearest neighbor.

Table 3: Molecule-molecule interaction potential (E_{MM}) as defined for the first five nearest neighbors. The potential is computed by the COMPASS forcefield. The last column (E_{cum}) indicates the cumulative contribution to cohesive energy due to all E_{MM} within the given neighbor distance, and displays a smooth saturation toward the bulk lattice energy E_{Lat} = -38.8 kcal/mol. Experimental lattice energy is -36.3 kcal/mol.

Neighbor shell # (i)	Neighbor lattice index	Neighbor dist (Å)	# Neighbors (Z_i)	$E_{MM}(i)$ (kcal/mol)	$E_{cum}(i)$ (kcal/mol)
1	0 0 1	6.71	2	-9.86	-5.4
2	½ ½ ½	7.43	8	-6.81	-32.6
3	1 0 0	9.38	4	-0.47	-33.5
4	0 1 1	11.53	8	-0.59	-35.9
5	½ ½ 3⁄2	12.05	8	-0.47	-37.8

2.2. KMC Simulations

2.2.1 Coarse Graining Procedure

As mentioned before, we substitute the entire PETN molecule, $C(CH_2ONO_2)_4$, by a single unit whose interaction depends on its local environment, i.e., number and type of neighbors, as shown in Fig. 10. This allows us to substitute the complexity of the 29 atoms that form a PETN molecule by an equivalent unit that is packed on a body center tetragonal lattice. These new PETN units interact according to the values given in Table 3. At each MC step, a particle is chosen at random and moved to a randomly chosen unoccupied site within a given cutoff radius. Next, we calculate the change of energy, ΔE, due to this move. The new configuration is accepted with probability 1 if the resulting energy change $\Delta E \leq 0$, and accepted with a probability $\exp(-\Delta E/K_B T)$ otherwise. This *local* random walk can be interpreted as the result of a few successive neighboring hops. As it is known, such procedure ensures that all possible configurations can be sampled if all attempted steps obey detailed balance (so no bias other than energy fluctuations occur). A more accurate approach would involve representing the above random walk as a product of successive neighboring diffusional steps weighted by the respective activation barriers. This would require the calculation of a large number of possible diffusion pathways, the corresponding transition states, and hopping rates.

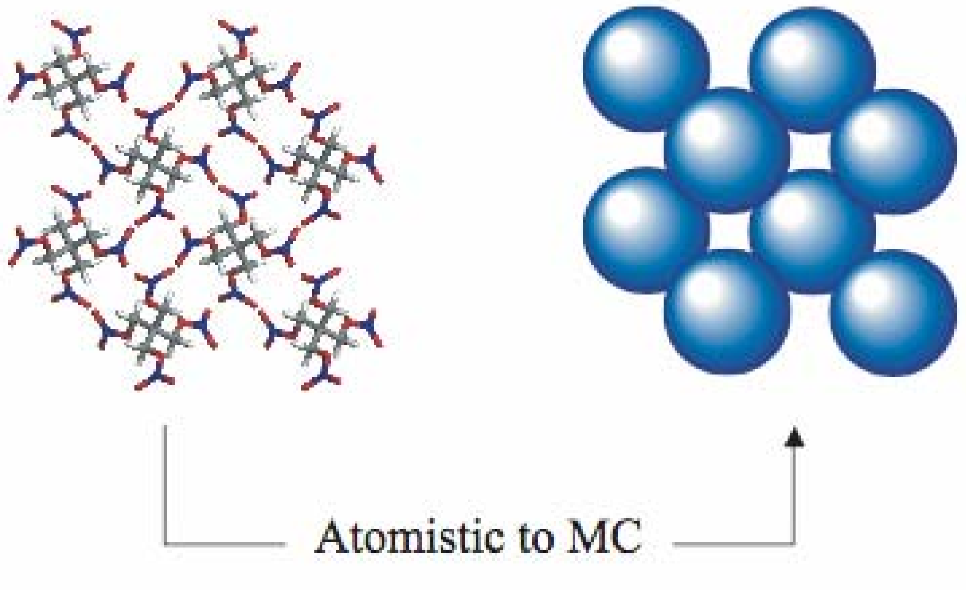

Figure 10. Coarse-graining of PETN into molecular units.

2.2.2 Growth Simulations of Single PETN Crystals

The influence of crystallographic anisotropy on the growth and evolution of PETN crystals is most clearly observed in the case of full three-dimensional systems in which all crystallographic orientations are accessible for deposition. As a first step in our analysis of size and habit evolution, we decided to study the evolution of the shape of a PETN crystal starting from an arbitrary initial shape. Fig. 11 displays the specific example when a *spherical* crystallite of diameter 16 nm is equilibrated for a sufficient number ($2x10^6$) of MC steps. The reason for choosing a sphere was to eliminate any directional bias or artificial anisotropy that might influence the resulting crystallite shape. The resulting configuration, Fig. 11(b) shows the presence of {101} and {110} facets, also present in the Hartman-Perdok morphology of Fig. 9(a). In addition, four small {100} faces are also present. These {100} faces can be interpreted as a collection of {110} step edges that have not yet meet. Note the comparable surface energies (obtained by COMPASS calculations) between these 3 faces: 0.22, 0.29 and 0.28 kcal/$Å^2$ for the {110}, {101}, and {100} surface, respectively. Thus, the appearance of these facets in the equilibrated structure gave us confidence not only on the accuracy of the inter-molecular lattice potential, but also its ability to mimic realistic crystallite shapes when used with the MC procedure described above.

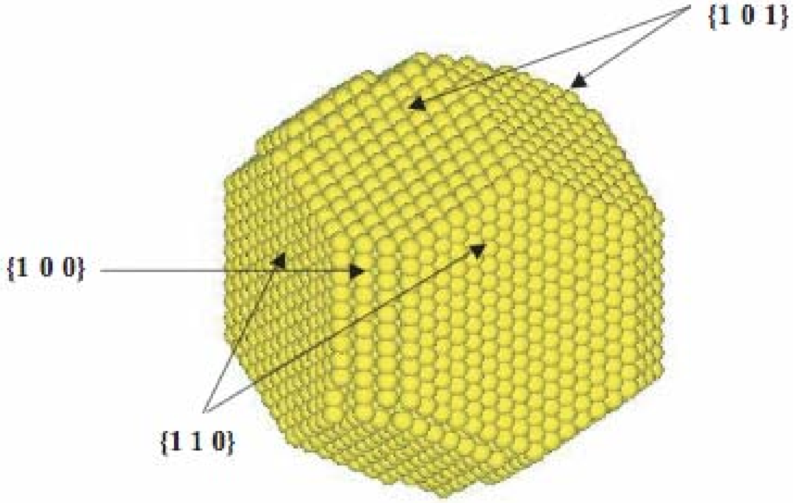

Figure 11. KMC computed shape after an initially spherical seed of diameter 16 nm is allowed to equilibrate.

The morphology in Fig. 11 results from the "local rearrangement" of a fixed number of particles (the ones that formed the initial spherical crystallite) driven by the tendency of the system energy to reach a local minimum. However, the experimentally observed morphologies are a result of growth through particle addition and diffusion, whose rates strongly depend on experimental conditions. To this end, we have studied the change in morphology during growth in a similar way as described in Ref. [7]. Thus, we start from an initial spherical seed, and add particles to the surface of the growing crystallite along a randomly selected radial direction [7]. Following each particle addition we perform a pre-defined number of MC steps, aimed at representing surface diffusion. Thus the above number of MC steps between two successive particle addition events represents, on an average, the ratio of diffusion rate to the growth rate of the crystallite.

Figure 12 shows the evolution of an initial spherical seed of 5 nm in diameter at 300 K. We performed 17 MC steps per insertion and particles were allowed to move within a cutoff radius of 5 nm. After insertion of only 200 particles, as shown in Fig 12(b), the surface of the crystal is covered by {101} and {110} facets of approximately the same size. As more material is added to the crystal, {110} facets become dominant as shown in Fig. 12(c). This is a result of the difference in adatom potential energy between these two faces. The {101} faces have lower adatom potential energy than the {110} faces, thus making the nucleation of new layer easier and leading to a faster growth, as shown in Fig. 12(d). As the crystal grows larger, the {110} facets can nucleate stable two dimensional islands that allow these faces to grow through the formation of multiple layers, as shown in Fig. 12(e).

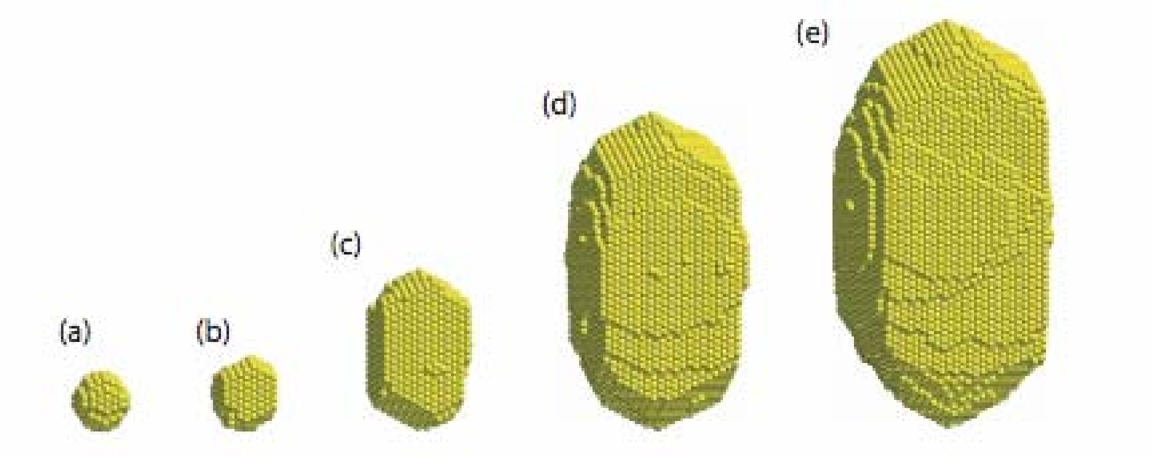

Figure 12. Shape evolution of PETN crystal with KMC. (a) initial spherical seed (diameter 5 nm); and after addition of (b) 2×10^2 molecules, (c) 2×10^3 molecules, (d) 1.5×10^4 molecules and (e) 3×10^4 molecules.

Controlling the relative ratio between the {101} and {110} facets can be achieved by varying experimental conditions such as growth rate and growth temperature. These experimental conditions will ultimately change the value of diffusion on each surface. Due to the lack of knowledge of these values, we incorporated such effect by varying the number of MC steps between insertions of new particles. Figure 13 shows the resulting configurations after $3.5\text{x}10^4$ particle insertions for 5, 10, 25, 50 and 100 MC steps between insertions in 6(a), 6(b), 6(c), 6(d), and 6(e), respectively. This variation can be interpreted either as an increase in surface diffusivity (e.g., by increasing the growth temperature) or as a decrease in growth rate.

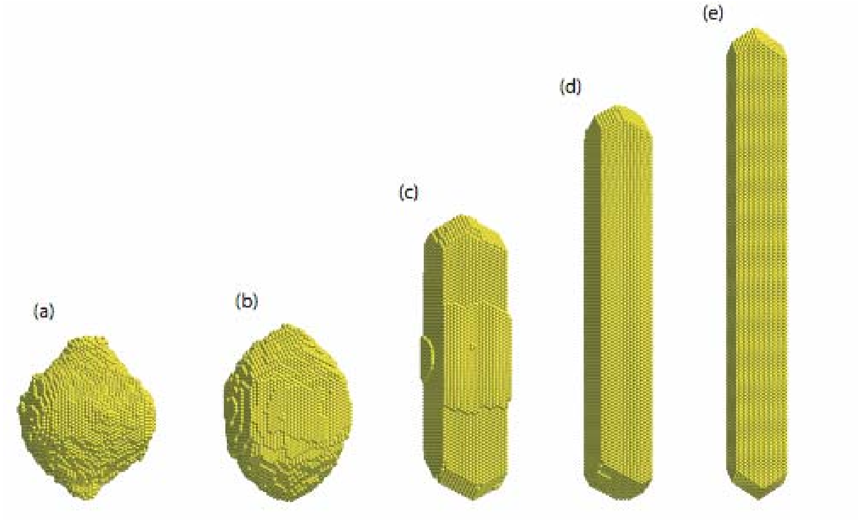

Figure 13. Comparison of the final configurations obtained after deposition of 3.5×10^4 particles on a spherical seed with (a) 5 MC cycles, (b) 10 MC cycles, (c) 25 MC cycles, (d) 50 MC cycles, and (e) 100 MC cycles between particle insertion.

2.2.3 Morphology Evolution of PETN Surface

In addition to examining the morphology evolution of single PETN crystals, we also modeled the evolution of island like features on a {110} PETN surface in order to compare with recent AFM experiments. The AFM images, although not definitive, had some features, which lead us to believe that the underlying mechanism was primarily a sublimation process. To test this hypothesis, we carried out KMC simulations where only sublimation events were considered. The relative sublimation frequencies were determined using the calculated desorptions energies listed in Table 4. Figure 14 shows the comparison of our PETN modeling results to AFM measurements. We specifically compared the dissolution of a specific island in the AFM image with a similar island in our simulations (circled regions in Figure 14). Both AFM measurements and KMC simulations show similar morphology changes, which point to sublimations being the dominant mechanism, although other interpretations are possible (see section 1.3), specifically, step bunching can play a critical role in the overall surface morphology changes seen in the AFM experiments. To this end, we have performed KMC simulations of a PETN {110} surface to elucidate the effects of impurities on the creation of step bunches. As is seen from our simulation results (Figure 15) the step velocity is substantially lowered as compared to the step velocity where no impurities are present. Thus, as stated earlier (section 1.3), it is likely that the estimation of the mobile step density in the AFM measurements may be too high, perhaps significantly. Further effort in the development of our PETN model is necessary to determine whether surface diffusion plays a dominant role here.

Table 4: Desorption energy as a function of crystallographic orientation, number of bond sites, and step configuration, in units of kcal/mol. Energies are computed using the COMPASS force field.

Face:	"(100)"	"(010)"	"(001)"	"(011)"	"(101)"	"(110)"	"(111)"
4 Bond Sites							
Bulk				-73.2	-60.5		
4 Planar Nearest Neighbors:					-60.3		
3 Bond Sites							
Along u/v:				-56.9	-47.0		
Diagonal wrt. u, v:				-53.6	-54.1		
2 Bond Sites (Kink)							
Along u/v, Filled:					-46.6		
Along u/v, Isolated:				-46.3	-46.5		
Diagonal wrt. u, v, Filled:				-46.6	-46.3		
Diagonal wrt. u, v, Isolated:							
1 Bond Site							
Along u or v:				-36.1	-45.8		
Diagonal:				-38.9	-38.8		
0 Bond Sites				-19.9	-30.5		

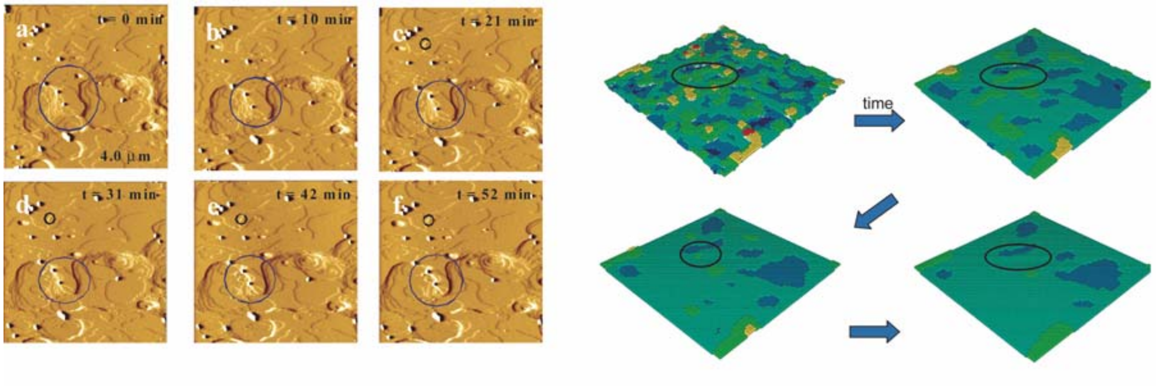

Figure 14. Time evolution of {110} PETN surface in air at 30 ^{o}C; comparison of AFM measurements (yellow surfaces) to KMC simulations of our model PETN (green surfaces).

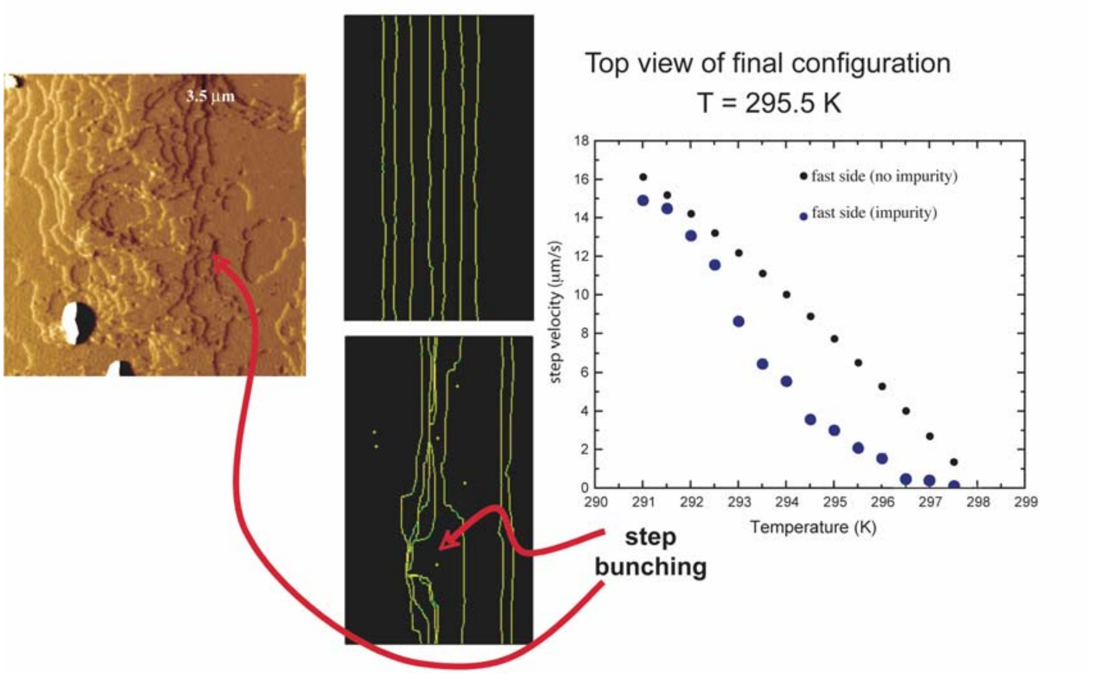

Figure 15. KMC simulations of the effect of step bunching on the step velocity as a function of temperature.

2.2.4 Evolution of PETN Powder Morphology (multi-crystallite simulations)

The next step towards developing a predictive lifetime assessment model for the coarsening known for PETN powders is to model nucleation/aggregation of PETN crystals. As a preliminary step towards this goal, we studied the evolution of different distributions of PETN crystallites using our KMC model, where no diffusion mechanism was considered. We used two different initial distributions: the first one is isolated PETN molecules randomly placed on the simulation cell and the second one is a collection of clusters of PETN molecules also randomly placed on the simulation cell. The cell was 47nm x 47nm x 40nm in size. We used periodic boundary conditions in the three directions. Three different coverages were used for each distribution: 0.3, 1.5 and 3. All initial configurations were annealed for 50×10^6 MC steps. Figures 16(a)-(f) show the initial and final configuration obtained for individual PETN molecules. Figures 17(a)-(f) show the initial and final configuration obtained for clusters of PETN molecules.

Future work will involve incorporating surface diffusion mechanisms of PETN molecules on various exposed surfaces, which will necessitate the computation of appropriate activation energy barriers from first principles, and their incorporation into the KMC code. This will also allow us to model the morphology changes in the presence of inhibitor molecules like tri-peon, iron, and other cations. Further, it is hoped that realistic densification and shrinkage of PETN powders can be realized in our simulations.

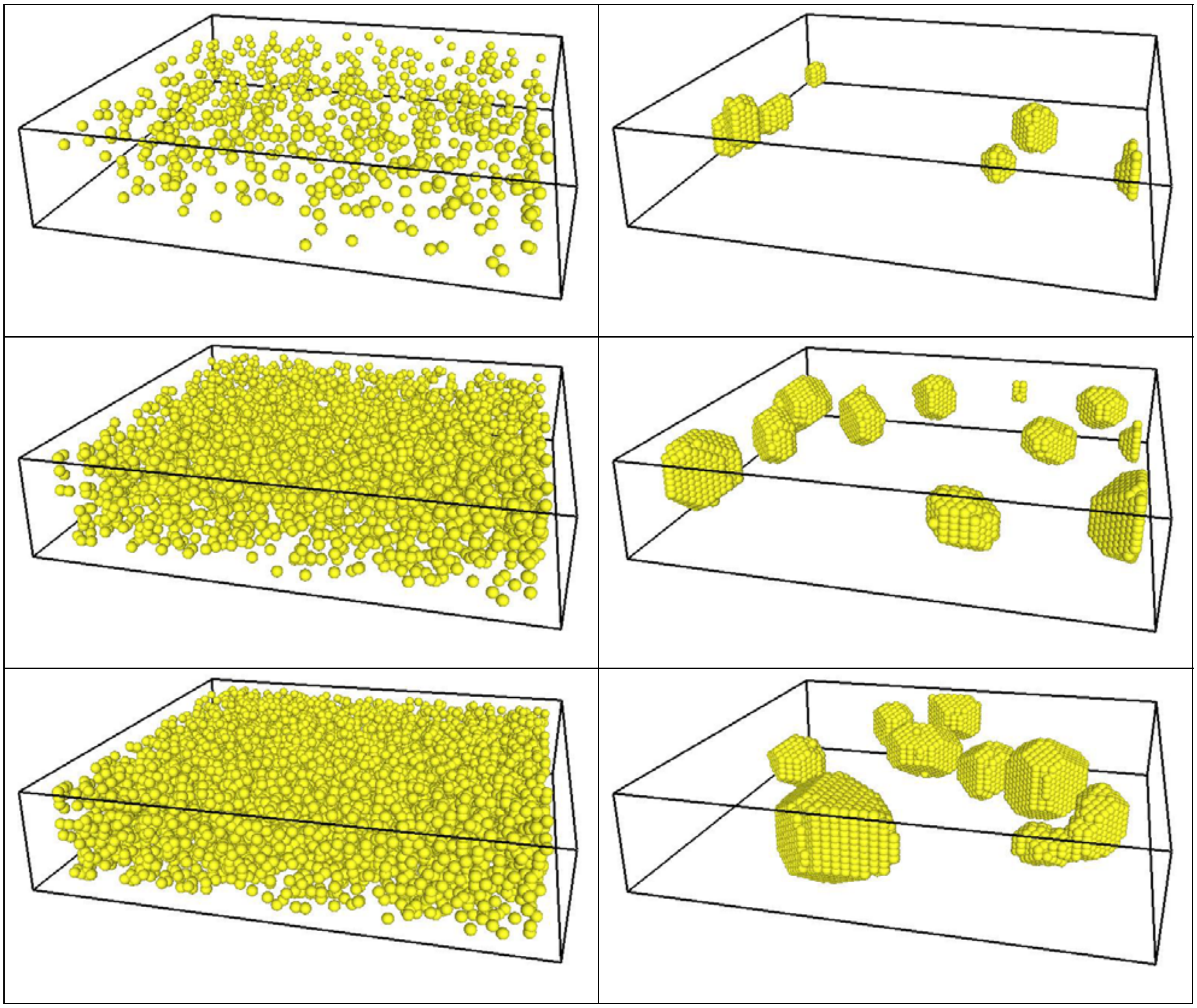

Figure 16. Evolution of a distribution of randomly placed individual PETN molecules. Initial and final configurations are shown for coverages of 0.3, 1.5, and 3 in (a) - (b), (c) - (d), and (e) - (f), respectively. All configurations were annealed for $5\text{x}10^6$ MC steps.

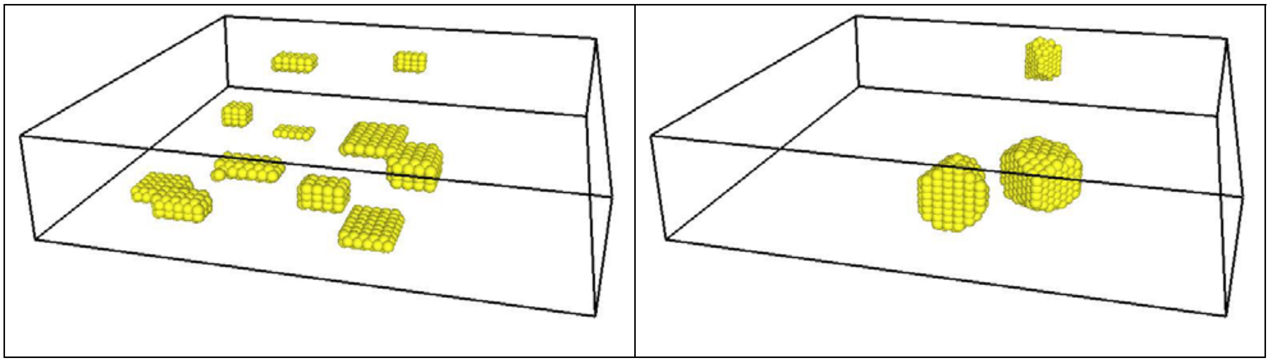

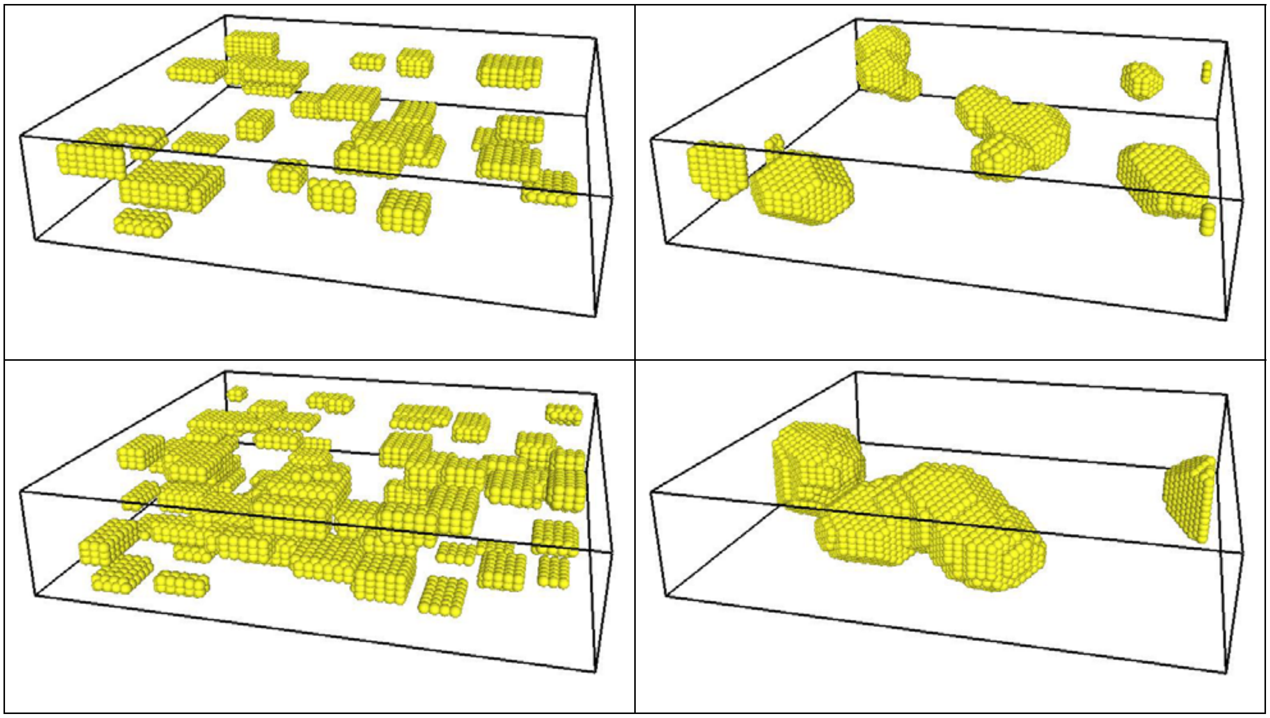

Figure 17. Evolution of a distribution of randomly placed clusters of PETN molecules. Initial and final configurations are shown for coverages of 0.3, 1.5, and 3 in (a) - (b), (c) - (d), and (e) - (f), respectively. All configurations were annealed for $5x10^6$ MC steps.

References:

1. Richard Behrens, **“**Update on the Analysis of Thermally and Chemically Stabilized PETN Powders,” *Presented at JOW0G Focused Exchange Meeting, May 12-14, 2003, Albuquerque, NM, Sandia National Laboratories*
2. H. Sun, J. Phys. Chem. B 102 (1998) 7338.
3. J. Trotter, Acta Crysta 16 (1963) 698.
4. J. S. Chickos, Heats of sublimation, in: J. F. Liebman, A. Greenberg (eds.), Molecular Structure and Energetics, VCH Publishers, New York, 1987, chapter 2.
5. G. Edwards, Trans. Faraday Soc. 49 (1953) 152.
6. P. Hartman, W. G. Perdok, Acta Cryst. 8 (1955) 49.
7. H. Huang, G. H. Gilmer, T. Diaz de la Rubia, J. Appl. Phys. 84 (1998) 3636.